

# Effects of Inlet Incidence Perturbations on Compressor Cascade Performance using Adaptive Sparse Grid Collocation

Z. Guo, W. Chu<sup>†</sup> and H. Zhang

*School of Power and Energy, Northwestern Polytechnical University, Xi'an, 710072, China*

<sup>†</sup>Corresponding Author Email: [wlcchu@nwpu.edu.cn](mailto:wlcchu@nwpu.edu.cn)

(Received October 28, 2022; accepted February 1, 2023)

## ABSTRACT

The effects of inflow variations due to the working environment and flight attitude changes on turbomachines are considerable in the real world. Nevertheless, uncertainty quantification can be adopted to assess mean performance changes and perform the aerodynamic shape design as well as optimization. Thus, an uncertainty quantification method of adaptive sparse grid collocation (ASGC) was first introduced to address the inflow uncertainties' effect issue effectively and accurately. Then, ASGC was utilized to evaluate the impacts of inlet incidence perturbations at different perturbation scales and reference inflow Mach numbers on the aerodynamic performance of a controlled diffusion cascade. The results showed that compared with the Monte Carlo simulation and static sparse grid collocation, the statistical accuracy and response accuracy of ASGC were maintained, and meanwhile its model construction efficiency was significantly improved because of the nested adaptive sampling feature. Under the perturbations of inlet incidences with high reference incidences, the mean aerodynamic loss always aggravates. The changes in aerodynamic loss nonlinearly depend on the inlet incidence perturbations, and the nonlinear dependence becomes greater when the perturbation scale expands. At the same perturbation scale, the nonlinear dependence on the inlet incidence perturbations is further enhanced when the reference inflow Mach number rises. Finally, uncertainty quantification of the flow field revealed that the fluctuation of flow accelerations at the leading edge plays a fundamental role in determining the uncertainty of the aerodynamic loss.

**Keywords:** Uncertainty quantification; Turbomachinery blade; Adaptive sparse grid collocation method; Aerodynamic performance; Inlet flow uncertainties.

## NOMENCLATURE

ASGC	Adaptive Sparse Grid Collocation	NIPRC	Non-Intrusive Probabilistic Collocation
$A$	Sparse grid interpolation process	PDF	Probability Density Function
$B$	relative hierarchical surplus	PS	pressure surface of blade
$c$	chord of blade [mm]	Stdv	statistical standard deviation
CDF	Cumulative Distribution Function	$S_g$	entropy generation
$D$	dimension of random input	SS	suction surface of blade
$H'_D$	sparse grid interpolation grids	SSGC	Static Sparsegrid Collocation
$H$	boundary layer shape factor	TE	trailing edge of blade
$L'_j$	interpolation basis functions	$U$	univariate interpolation process
$L$	total pressure loss coefficient	UQ	uncertainty quantification
$l$	interpolation level	$\alpha$	inlet incidence
$l_{max}$	maximum interpolation level	$\beta_{1k}$	inlet metal angle
LE	leading edge of blade	$\delta$	variation relative to the nominal
$Ma_1$	inflow Mach number	$\epsilon_0$	interpolation error tolerance
$Ma_{is}$	isentropic Mach number	$\epsilon_{ave}$	mean of response error
MCS	Monte Carlo simulation	$\epsilon_{rms}$	standard deviation of response error
$m$	number of 1- $D$ interpolation nodes	$\mu$	statistical mean value
$N$	number of training samples	$\sigma$	statistical standard deviation
NIPC	Non-Intrusive Polynomial Chaos	$\omega$	hierarchical surplus

## 1. INTRODUCTION

There are many uncertainties either in the real world or at the inlet of turbomachines, such as geometric variations (Garzon and Darmofal 2003, 2004), and flow variations (Stenning 1980; Bry *et al.* 1985). They usually lead to undesirable aerodynamic performance deterioration. It is of great significance for the robust design of turbomachinery to evaluate the effect of uncertain inducements on performance. An effective approach to improving the robustness of actual aerodynamic performance is to use an uncertainty quantification (UQ) method for analysis and design.

In the last century, performance changes of turbomachinery blades were measured through experiments (Bammert and Sandstede 1976; Roelke and Haas 1983). In the past decades, many studies applied Monte Carlo simulation (MCS) to evaluate the impact of machining deviations on the performance of turbomachinery blades (Garzon and Darmofal 2003, 2004; Lange *et al.* 2010, 2012). Compared with the defects of long cycles and high costs exposed in the early experimental method, MCS can perform UQ of aerodynamics in a quick and accurate manner. With the increasing complexity of aerodynamic shapes and uncertain inducements, sensitivity analysis methods (Putko *et al.* 2002; Luo and Liu 2018) such as the method of moment and the probabilistic models (Xiu and Karniadakis 2003; Loeven *et al.* 2007; Hosder *et al.* 2010; Loeven and Bijl 2010; Liu *et al.* 2014; Panizza *et al.* 2014; Seshadri *et al.* 2015; Wunsch *et al.* 2015; Ahlfeld and Montomoli 2017; Wang and Zou 2019; Xia *et al.* 2019a) have been developed rapidly in the recent decade, further improving the efficiency of MCS. By using the method of moment, Putko *et al.* (2002) determined the uncertainty propagations of geometric and flow variations separately in the quasi-one-dimensional flow. Luo and Liu (2018) further investigated the impact of manufacturing variations on a turbine cascade using the second-order adjoint sensitivity analysis. In contrast with MCS results, the sensitivity analysis methods showed obviously high precision and great efficiency. However, the sensitivity-based methods are only suitable for small-scale stochastic problems (Xia *et al.* 2019a). For large-scale aerodynamic stochastic issues, the probabilistic models shall be outweighed because of their global characteristics.

Among those methods available for establishing the probabilistic models, non-intrusive polynomial chaos (NIPC) (Xiu and Karniadakis 2003) and non-intrusive probabilistic collocation (NIPRC) (Loeven *et al.* 2007) are the most popular due to their outstanding capabilities in rapid convergence. Moreover, Computational Fluid Dynamics (CFD) is regarded as a black box model requiring no change of the CFD program codes in non-intrusive methods. NIPC is based on the spectral representation of the uncertainty. Once the spectral representation is constructed with a certain number of training samples, function responses can be determined, and then the statistics are directly inferred from the PC coefficients, which have been widely used in

aerodynamic UQ of turbomachinery blades (Loeven *et al.* 2007; Hosder *et al.* 2010; Panizza *et al.* 2014; Seshadri *et al.* 2015; Ahlfeld and Montomoli 2017; Wang and Zou 2019). In NIPRC, collocation points are chosen according to Gauss quadrature nodes, and the probability distribution of the solution is constructed with Lagrange interpolation. The results in the reference (Loeven *et al.* 2007) demonstrated that for the same amount of computational cost, the accuracy of the NIPRC methods was higher than that of the NIPC methods. By using NIPRC, Loeven and Bijl (2010) investigated the impact of an uncertain inlet total pressure profile on the performance of a transonic compressor rotor - NASA Rotor 37. Liu *et al.* (2014) studied the effects of inlet velocity uncertainties on the aerodynamic performance of a wind turbine. Wunsch *et al.* (2015) explored the impact of the coexistence of the operation and geometric uncertainties on Rotor 37. Nevertheless, the collocation nodes in NIPRC are not nested, i.e., low-order collocation nodes cannot be reused in the construction of a higher-order probabilistic model, resulting in a huge waste of samples.

In practical engineering, a low-order quadrature formula is often constructed first, and then the approximation accuracy is improved with the increase of the order of the quadrature formula. The nested quadrature rules, such as the Kronrod-Patterson-Hermite quadrature rule (Liao *et al.* 2017), indicate that the lower-order quadrature nodes can be reused in a higher-order scheme. Moreover, Heiss and Winschel (2008) provided the readily calculated matrices of nodes and weights for nested quadrature rules. Based on the extended Gauss-Hermite nested quadrature rule (Genz and Keister 1996), Wang *et al.* (2020) developed a new sparse grid collocation method for UQ of the impact of stagger angles on the performance of a turbine blade. However, not all the collocation nodes added in the construction of high-order probability models need to be utilized. The reinforcement of the collocation nodes near the smooth or flat area of the real response also leads to a waste of samples. To alleviate the computational burden for aerodynamic UQ to the maximum extent, an ASGC method is introduced in this paper. It should be noticed that there is an existing ASGC method (Conrad and Marzouk 2013) reducing the training samples based on the dimension-adaptive quadrature approaches. In the current study, the proposed ASGC still has the nested property, and can dynamically add collocation nodes with increasing collocation levels, thereby further minimizing the computational costs of highly accurate probabilistic surrogate modeling.

Nowadays, there has been much publicly available literature working on UQ of performance for turbomachinery blades concerning the effects of inlet flow variations with a single fluctuation range (Gopinathrao *et al.* 2009; Loeven and Bijl 2010; Liu *et al.* 2014; Wunsch *et al.* 2015; Xia *et al.* 2019b). In most cases, the fluctuation scale of inlet flow variables varies with the working environment of turbomachines. The effects of different fluctuation scales on aerodynamic performance are worth further quantifying. Besides, being affected by the

flight attitude, the reference operation conditions are constantly changing. Thus, the effects of inlet flow variations at different reference operation conditions must be considered during the statistical analysis. Additionally, to lay the foundation for further improving the aerodynamic robustness of blade shapes, UQ studies should be performed covering the influence mechanism of stochastic inflow variations at different fluctuation scales and reference operation conditions on aerodynamics.

In the present study, according to the proposed ASGC method, aerodynamic UQs of a subsonic aero-engine compressor cascade were carried out. Specifically, the loss uncertainty concerning incidence perturbations was quantified, and the influence law of incidence perturbations on the loss uncertainty at different scales and inflow Mach numbers was analyzed. Finally, the key factor for triggering the uncertainty of the cascade flow field was discussed in detail using UQ. The applicable methods and conclusion will provide certain guidelines for the aerodynamic UQ and design of real compressor blades.

## 2. ADAPTIVE SPARSE GRID COLLOCATION

### 2.1 Smolyak Sparse Grid Algorithm

Smolyak sparse grid algorithm provides a method to construct interpolation formulas based on a minimal number of nodes in multivariate space. The algorithm has already been introduced in the open literature (Gerstner and Griebel 1998; Barthelmann *et al.* 2000) and below is a quick review.

For a univariate function  $f: [0, 1] \rightarrow \mathbb{R}$ , the univariate interpolation formula is

$$U^i(f) = \sum_{j=1}^{m_i} f(x_j^i) L_j^i(x), \quad (1)$$

where  $i$  is the interpolation depth,  $m_i$  is the number of the interpolation nodes,  $x_j^i$  and  $L_j^i$  represent the interpolation nodes and basis functions, respectively. In multivariate cases, the full tensor product formula used to approximate the function  $f: [0, 1]^D \rightarrow \mathbb{R}$  is

$$\begin{aligned} & (U^{i_1} \otimes \dots \otimes U^{i_D}) \\ &= \sum_{j_1=1}^{m_{i_1}} \dots \sum_{j_D=1}^{m_{i_D}} f(x_{j_1}^{i_1}, \dots, x_{j_D}^{i_D}) \cdot (L_{j_1}^{i_1} \otimes \dots \otimes L_{j_D}^{i_D}). \end{aligned} \quad \dots(2)$$

However, the total number of interpolation nodes required to construct Eq. (2) increases exponentially with dimension  $D$ . To mitigate this issue, the Smolyak sparse grid algorithm uses a much smaller subset of the full tensor grid (Smoljak 1963) to carry out the interpolation:

$$A_{l,D}(f) = \sum_{l+1 \leq |\mathbf{i}| \leq l+D} (-1)^{l+D-|\mathbf{i}|} \binom{D-1}{l+D-|\mathbf{i}|} \cdot (U^{i_1} \otimes \dots \otimes U^{i_D}), \quad (3)$$

where  $l$  indicates the sparse grid level, and the multi-index set  $\mathbf{i} = (i_1, i_2, \dots, i_D)$  satisfies  $|\mathbf{i}| = i_1 + i_2 + \dots + i_D$ .

The sparse grid interpolation grids  $H_D^l$  generated by the Smolyak algorithm are

$$H_D^l = \bigcup_{l+1 \leq |\mathbf{i}| \leq l+D} \Theta^{i_1} \otimes \Theta^{i_2} \dots \otimes \Theta^{i_D}, \quad (4)$$

where  $\Theta^i = \{x_1^i, \dots, x_m^i\}$  is the 1- $D$  interpolation nodes for  $U^i$ . The sparse grid interpolation accuracy is  $O(N^{-2} \cdot (\log N)^{D-1})$  with respect to the maximum norm where  $N$  is the number of nodes used.

### 2.2 Adaptive Algorithm

The difference is calculated by  $\Delta^i = U^i - U^{i-1}$  with  $U^0 = 0$ , and the  $D$ -dimensional and  $l$ -level interpolation formula as in Eq. (3) can be rewritten in a hierarchical form:

$$\begin{aligned} A_{l,D}(f) &= \sum_{|\mathbf{i}| \leq l+D} (\Delta^{i_1} \otimes \dots \otimes \Delta^{i_D})(f) \\ &= A_{l-1,D}(f) + \sum_{|\mathbf{i}| = l+D} (\Delta^{i_1} \otimes \dots \otimes \Delta^{i_D})(f). \end{aligned} \quad (5)$$

Once the nested nodes are selected for  $\Theta^i$ , i.e.,  $\Theta^i \subset \Theta^{i+1}$ , only the calculation of the function responses at  $\Theta_{i,\Delta} = \Theta^i \setminus \Theta^{i-1}$  is needed to extend the interpolation depth from  $i-1$  to  $i$ . On this condition, when the interpolation level is increased from  $l-1$  to  $l$  in  $D$  dimensions, only the responses at differential grids need calculating with  $\Delta H_D^l$  given by

$$\Delta H_D^l(f) = \bigcup_{|\mathbf{i}| = l+D} (\Theta_{i,\Delta}^{i_1} \otimes \dots \otimes \Theta_{i,\Delta}^{i_D}). \quad (6)$$

Because of this nested characteristic, Eq. (5) can be further simplified as

$$\begin{aligned} A_{l,D}(f) &= A_{l-1,D}(f) + \sum_{|\mathbf{i}| = l+D} \sum_{\mathbf{j} \in \mathbf{V}_i} (L_{j_1}^{i_1} \otimes \dots \otimes L_{j_D}^{i_D}) \times \\ & (f(x_{j_1}^{i_1}, \dots, x_{j_D}^{i_D}) - A_{l-1,D}(f)(x_{j_1}^{i_1}, \dots, x_{j_D}^{i_D})), \end{aligned} \quad (7)$$

where  $\mathbf{V}_i = \{\mathbf{j}: x_{j_r}^{i_r} \in \Theta_{i,\Delta}^{i_r} \text{ for } j_r = 1, \dots, m_{i_r}, r = 1, \dots, D\}$  is the index set for new nodes generated at the depth  $i_r$ ,  $m_{i_r} = m_{i_r} - m_{i_r-1}$ . In this study, the nested Newton-Cotes grid and the piecewise linear hat function are used in the adaptive algorithm due to their excellent local adaptivity (Ma and Zabarar 2009).

For some large-scale perturbations of inflow variables at the near-stall condition, such as the high incidence of compressor blades, the deterministic CFD solutions on the perturbation boundary are sometimes difficult to converge, or the convergence curve of CFD solutions fluctuates greatly. In this instance, the CFD results at the near-stall condition may not be valid. To make UQ results reliable, the grids on the boundary must be omitted. Herein, the one-dimensional Newton-Cotes nodes with boundary nodes removed are defined as follows:

$$x_j^i = \begin{cases} \frac{1}{2}, & \text{if } m_i = 1, \\ \frac{j}{m_i + 1}, & \text{if } m_i > 1 \text{ for } j = 1, \dots, m_i, \end{cases} \quad (8)$$

where the number of nodes is defined as  $m_i=2^{i-1}$ . Accordingly, the piecewise linear hat functions  $L_j^i$  should be modified to extrapolate linearly towards the boundary as follows:

$$\begin{aligned}
 &L_j^i(x)=1 \text{ for } i=1, \text{ and} \\
 &\text{if } j = 1, \\
 &L_j^i(x)=\begin{cases} 2-(m_i+1)\cdot x, & \text{if } x < 2/(m_i+1), \\ 0, & \text{otherwise,} \end{cases} \\
 &\text{if } j = m_i, \\
 &L_j^i(x)=\begin{cases} (m_i+1)\cdot x - m_i + 1, & \text{if } x < 2/(m_i+1), \\ 0, & \text{otherwise,} \end{cases} \\
 &\text{otherwise,} \\
 &L_j^i(x)=\begin{cases} 2-(m_i+1)\cdot x, & \text{if } x < 2/(m_i+1), \\ 0, & \text{otherwise,} \end{cases}
 \end{aligned} \tag{9}$$

To dynamically refine the grid locally as the level  $l$  increases, a hierarchical surplus  $\omega_j^{l,i}$  is defined to refer to the error between the exact function response and the interpolation result at the previous interpolation level of an interpolation node corresponding to the sets  $\mathbf{i}$  and  $\mathbf{j}$ :

$$\omega_j^{l,i} = f(x_{j_1}^i, \dots, x_{j_D}^i) - A_{l-1,D}(f)(x_{j_1}^i, \dots, x_{j_D}^i). \tag{10}$$

If the target function has an extreme value, marked fluctuations of the gradient, or highly nonlinear regions, a large hierarchical surplus value will be obtained. Therefore, the hierarchical surplus can be regarded as an error indicator for adaptive sampling (Griebel 1998). To avoid encrypting redundant grids where the real function is relatively smooth, we used relative hierarchical surplus  $B_j^{l,i}$  as an error indicator:

$$B_j^{l,i} = \frac{\omega_j^{l,i}}{\max_{j \in V_i} |f(x_{j_1}^i, \dots, x_{j_D}^i)|}. \tag{11}$$

The proposed ASGC method is conceptually introduced in Fig. 1. Compared to the existing adaptive strategy (Ma and Zabarar 2009), the proposed ASGC uses the collocation nodes with boundary nodes removed and the relative hierarchical surplus.

Once the interpolation formula constructed by the ASGC is determined, the Newton-Cotes quadrature weight  $w_i$  with  $i = 1, 2, \dots, N$  corresponding to the  $N$  adaptive sparse grid nodes used can be calculated. Therefore, the mean  $\mu_f$  and variance  $\sigma_f^2$  of the original function  $f$  can be computed by

$$\mu_f = \int_{[0,1]^D} f(\mathbf{x}) f_x(\mathbf{x}) d\mathbf{x} = \sum_{i=1}^N w_i f(\mathbf{x}^{(i)}) f_x(\mathbf{x}^{(i)}), \tag{12}$$

$$\begin{aligned}
 \sigma_f^2 &= \int_{[0,1]^D} [f(\mathbf{x}) - \mu_f]^2 f_x(\mathbf{x}) d\mathbf{x} = \\
 &\sum_{i=1}^N w_i [f(\mathbf{x}^{(i)}) - \mu_f]^2 f_x(\mathbf{x}^{(i)}),
 \end{aligned} \tag{13}$$

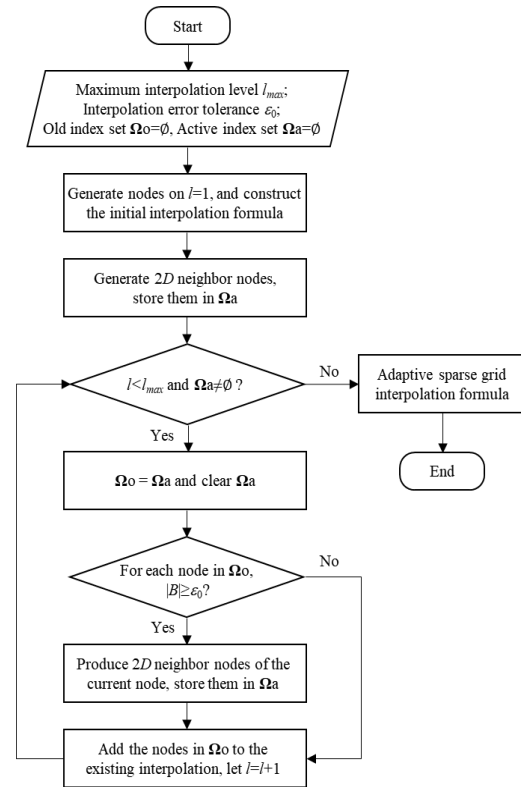


Fig. 1. Flowchart of the ASGC method.

where  $f_x(\mathbf{x})$  denotes the probability density function (PDF) of  $\mathbf{x} = (x_1, x_2, \dots, x_D)$ . Moreover, the PDF and cumulative distribution function (CDF) of the original function can be easily evaluated by performing MCS on the interpolation formula determined.

### 2.3 Function Test of ASGC

A nonlinear function test was performed to verify the response performance of ASGC, including the statistical accuracy, response accuracy, and model construction efficiency. The test function is

$$\begin{aligned}
 f(\mathbf{x} : x_1, x_2) &= \\
 &(\sin 10x_1 + \cos 3x_2^2) \cdot \cos 40x_2 \cdot (1 - e^{-x_1^4}),
 \end{aligned} \tag{14}$$

where  $x_1$  and  $x_2$  obey the truncated Gaussian distribution, which has a mean value of 0.5 and a  $\pm 0.5$  variability.

For comparison, static sparse grid collocation (SSGC) and MCS are considered. The MCS results are regarded as the exact solution for reference while the SSGC model is directly established by Eq. (7) without using the adaptive algorithm. To quantify the response accuracy of the sparse grid collocation, the mean error  $\varepsilon_{ave}$  and root mean square error  $\varepsilon_{rms}$  are defined as

$$\varepsilon_{ave} = \frac{1}{M} \sum_{i=1}^M |f(\mathbf{x}^{(i)}) - A_{l,D}(f)(\mathbf{x}^{(i)})|, \tag{15}$$

$$\varepsilon_{rms} = \sqrt{\frac{1}{M} \sum_{i=1}^M |f(\mathbf{x}^{(i)}) - A_{l,D}(f)(\mathbf{x}^{(i)})|^2}, \quad (16)$$

where  $M$  is the number of test samples generated by the direct MCS,  $f$  and  $A_{l,D}$  refer to the exact solution and the interpolation result, respectively.

Figure 2 compares the response errors  $\varepsilon_{avr}$  and  $\varepsilon_{rms}$  using different sparse grid collocations and indicates that much fewer points are needed in the ASGC than in the SSGC to achieve the same response accuracy. To be specific, Table 1 demonstrates the mean, standard deviation (Stdv), response errors, and numbers of training samples for the SSGC and ASGC. The mean and Stdv of the response obtained by sparse grid interpolation coincide with that in the MCS results. The mean, Stdv, and response errors for SSGC are close to that of ASGC which displays fewer training samples, further illustrating the feasibility of the adaptive sampling method in reducing the training samples.

Figure 3 shows the grid node evolution of the ASGC. The low-level grid nodes are reused in the construction of the interpolation formula with a higher level. Most of the nodes are distributed in the areas where large gradient changes of the function occur. These further embody that the proposed ASGC has the characteristics of nested adaptive sampling.

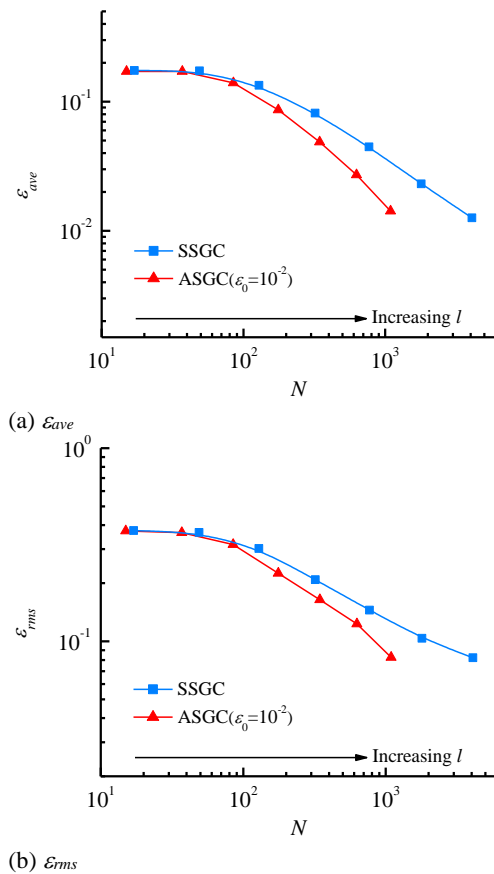


Fig. 2. Comparison of the response errors using different sparse grid collocations.

Table 1 Results of function experiments by MCS, SSGC ( $l=9$ ), and ASGC ( $l_{max}=9, \varepsilon_0=10^{-2}$ )

	MCS	SSGC	ASGC
$\mu_f$	$1.21 \times 10^{-4}$	$1.41 \times 10^{-4}$	$1.05 \times 10^{-4}$
$\sigma_f$	0.1784	0.1781	0.1780
$\varepsilon_{ave}$	-	$1.26 \times 10^{-2}$	$1.42 \times 10^{-2}$
$\varepsilon_{rms}$	-	$8.22 \times 10^{-2}$	$8.25 \times 10^{-2}$
$N$	10000	4097	1092

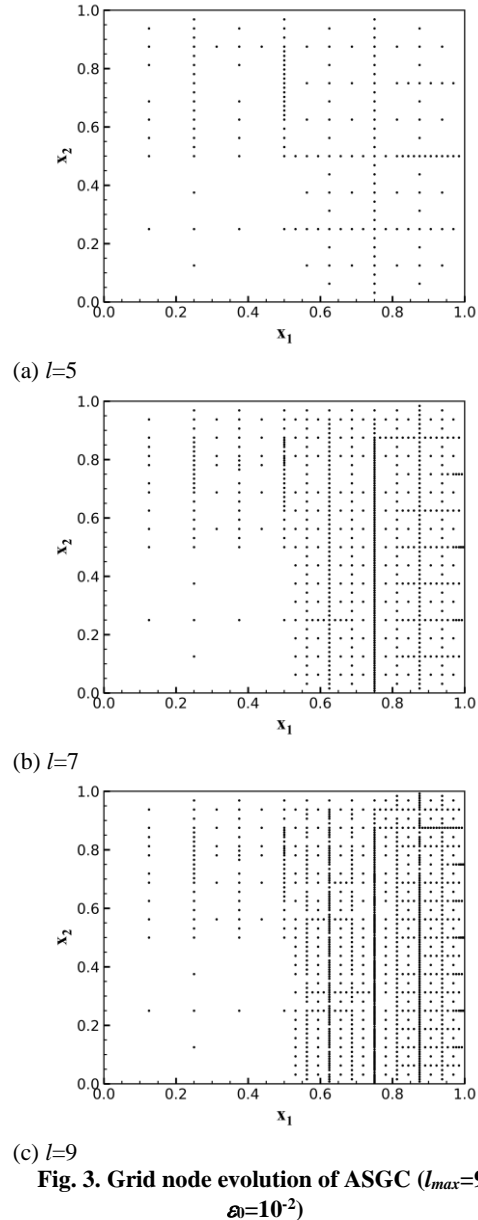


Fig. 3. Grid node evolution of ASGC ( $l_{max}=9, \varepsilon_0=10^{-2}$ )

### 3. UNCERTAINTY QUANTIFICATION OF THE IMPACT OF INLET INCIDENCE PERTURBATIONS

#### 3.1 Description of the Numerical Model

A subsonic compressor cascade, which was self-designed by Ma *et al.* (2017), is extracted as the specific research object in the following study. It is a controlled diffusion airfoil with a circular leading edge (LE) and trailing edge (TE), and its main

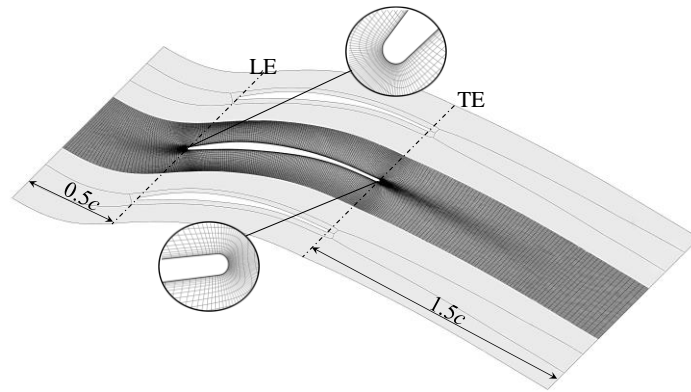


Fig. 4. Geometric configuration and local computational mesh of the cascade.

Table 2 Main geometric parameters.

Variables	Values
Radius of the leading edge (mm)	0.5205
Radius of the trailing edge (mm)	0.5850
Pitch (mm)	30.44
Inlet metal angle (deg)	45.83
Outlet metal angle (deg)	6.22
Chord length $c$ (mm)	69.95
Stagger angle (deg)	26.58

geometric parameters are provided in Table 2. The inlet flow angle is 47.83 degrees (deg) and the design incidence is 2.5 deg.

Figure 4 shows the cascade's geometric configuration and local computation mesh. The inlet and outlet domains are respectively extended to 0.5 chords upstream of the LE and 1.5 chords downstream of the TE. The domain is meshed using an "O4H" block topology to generate quadrangular structured grids. The "O" and "H" blocks are used to surround the blade and cover the upstream and downstream passages, respectively. The calculation mesh in a single flow passage has about 165,000 cells, and  $Y^+$  is about 1.0. The mesh has been verified to meet the requirement of grid independence through previous work (Guo and Chu 2022), and used for many aerodynamic studies (Guo *et al.* 2022a, b).

With NUMECA software, the Reynolds Average Navier-Stokes equations are used to calculate the single passage mesh with translation periods. The compressible ideal gas is the working medium, and the turbulence model is the Spalart-Allmaras model. The adiabatic wall with the no-slip assumption is defined on the solid surfaces. Turbulence viscosity  $0.001 \text{ m}^2/\text{s}$ , total pressure 101325 Pa, total temperature 288.15 K, and various incidences  $\alpha$  are imposed on the inlet.  $\alpha$  equals the inflow angle minus the inlet metal angle. The mass flow rate is given at the outlet to maintain the inflow Mach number  $Ma_1$ .  $Ma_1$  is defined as the vectorial sum of tangential and axial flow Mach numbers.

In Fig. 5, the numerical results of the isentropic Mach number  $Ma_{is}$  distribution on the cascade surface and the loss coefficient at  $1.0c$  downstream of the TE are validated with the experimental data in the reference

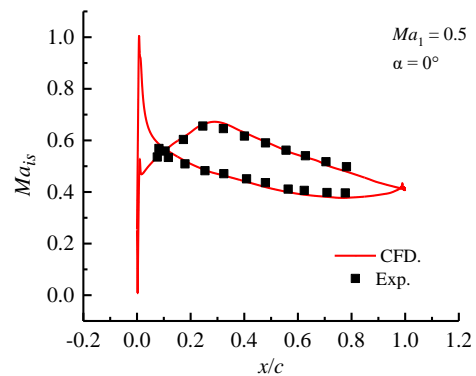
(Ma *et al.* 2017) and the comparison shows a good agreement.

### 3.2 Evaluations of Performance Impact

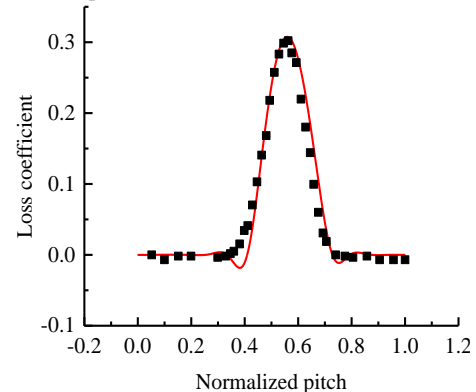
Total pressure loss coefficient  $L$  is used to evaluate the aerodynamic performance with the definition as follows:

$$L = \frac{P_{in}^* - P_{out}^*}{P_{in}^* - P_{in}}, \quad (17)$$

where  $p$  refers to pressure, superscript  $*$  refers to the total value, and subscripts *in* and *out* refer to the passage inlet and outlet, respectively.



(a) Isentropic Mach number



(b) Loss coefficient at  $1.0c$  downstream of TE

Fig. 5. Comparison between the numerical and experimental results.

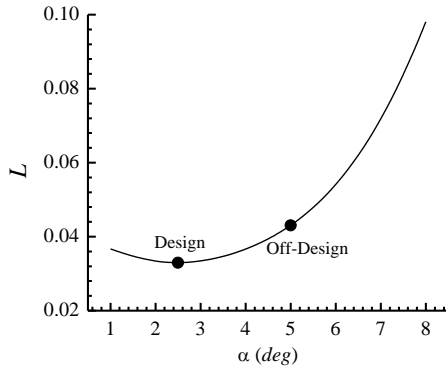


**Fig. 6. The  $L$  distribution at different inlet incidences when reference  $Ma_1=0.7$**

The  $L$  distribution with the inlet incidences when the reference  $Ma_1=0.7$  is first calculated as shown in Fig. 6. At the design condition,  $L$  varies as a flat quadratic curve, while at the off-design condition with high inlet incidences,  $L$  varies as an increasing cubic curve, implying that  $L$  is more sensitive to the variations of  $\alpha$  and less robust. To provide design guidance for effective improvement of the aerodynamic robustness of the cascades, this study concerned the inlet incidence perturbations at the off-design incidence  $\alpha=5$  deg, because the change of  $L$  is relatively more drastic afterward. Since the relative changes are more intuitive, the relative variation of the total pressure loss coefficient  $\delta L$  is employed to display the performance change. Many studies (Luo and Liu 2018, Xia *et al.* 2019b) have adopted this illustration, which is defined as

$$\delta L = \frac{L - L_0}{L_0}, \quad (18)$$

where  $L_0$  is the nominal value of the total pressure loss coefficient.

Gaussian distributions for flow variations have been widely applied in describing stochastic flow variations (Hosder *et al.* 2007; Loeven *et al.* 2007; Loeven and Bijl 2010). Because the disturbance range of uncertainty variables cannot be infinite, the truncated Gaussian distribution is more practical to describe the uncertainty, which has been accepted by many aerodynamic UQ studies (Wu *et al.* 2017; Guo and Chu 2022). Thus, it is also employed to illustrate the variation of inlet incidences

$$z = \frac{\alpha - \alpha_{ref}}{\sigma_\alpha}. \quad (19)$$

And its PDF is

$$f_z(z) = \begin{cases} \frac{1}{0.9974\sqrt{2\pi}} \exp\left(-\frac{z^2}{2}\right), & z \in [-3, 3], \\ 0, & \text{otherwise,} \end{cases} \quad (20)$$

where  $\alpha_{ref}=5$  deg and  $\sigma_\alpha$  is the Stdv of inlet incidence variation.

To investigate the effect of ASGC on the aerodynamic UQ results, the aerodynamics of the studied cascade was statistically evaluated at

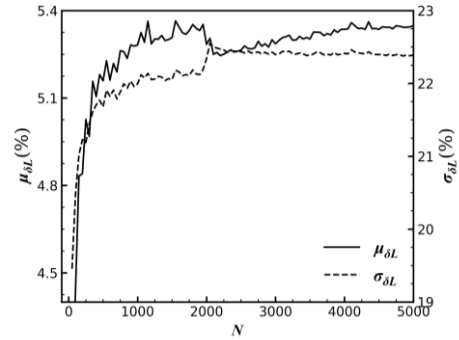


**Fig. 7. Convergence history of direct MCS-based statistics when reference  $Ma_1=0.7$  and  $\sigma_\alpha=1$ .**

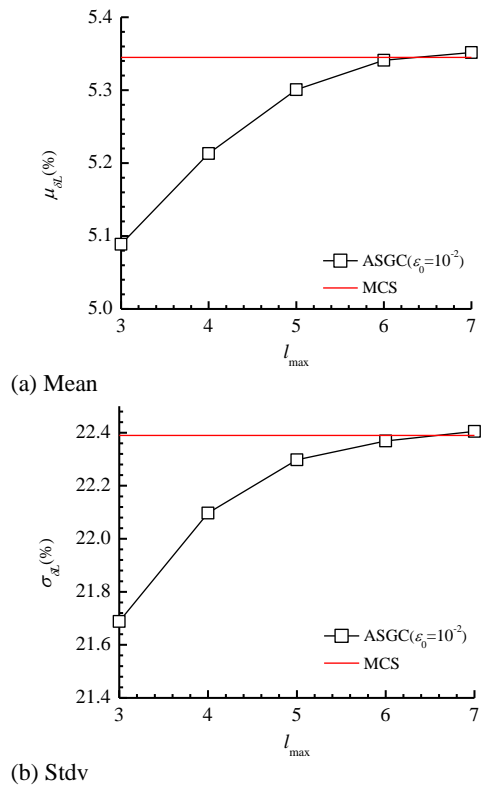


**Fig. 8. Statistical distribution of  $\delta L$  with the maximum interpolation level.**

reference  $Ma_1=0.7$  and  $\sigma_\alpha=1$ . Figure 7 shows the convergence history of the direct MCS-based statistics on  $\delta L$ . The mean and Stdv of  $\delta L$  are convergent once the number of trials exceeds 4,500. To maintain the accuracy of statistics, the 5,000 samples-based statistics are regarded as the exact ones in the following study.

We first studied the statistical convergence of ASGC by increasing the level  $l_{max}$ . Figure 8 shows the statistical result of  $\delta L$  with  $l_{max}$  of ASGC and the comparison with that of MCS. When  $l_{max}=6$  or 7, the result of ASGC coincides with that of MCS, showing few differences between ASGC and MCS. Then, the convergence of ASGC was also studied by increasing the tolerance  $\epsilon_0$ . Figure 9 presents the statistical result of  $\delta L$  with  $\epsilon_0$  of ASGC and the comparison with that of MCS. When  $\epsilon_0=10^{-2}$ , the result of ASGC coincides well with that of MCS.

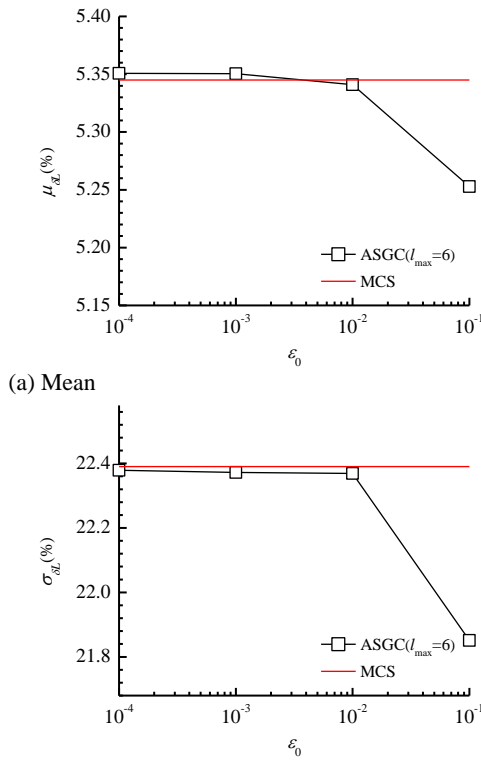


**Fig. 9. Statistical distribution of  $\delta L$  with the interpolation error tolerance.**

The overall comparison result indicates that the ASGC with  $l_{max} \geq 6$  and  $\epsilon_0 \leq 10^{-2}$  can better produce the statistics.

Lastly, the computational costs and response accuracy of ASGC were compared with that of SSGC, as shown in Table 3. Compared with MCS, the necessary CFD evaluations for ASGC and SSGC are significantly reduced. ASGC requires fewer CFD evaluations than SSGC with similar response accuracy, further indicating that the aerodynamic UQ efficiency can be improved by ASGC. From the second to fourth rows of the table, as  $l_{max}$  increases or  $\epsilon_0$  decreases, the number of training samples increases accordingly, while the function response accuracy changes lessen.

Therefore, the number of training samples can be maximally reduced for the ASGC with  $l_{max}=6$  and  $\epsilon_0=10^{-2}$  while response accuracy is still ensured.

PDF and CDF are widely applied to in-depth statistical analysis. Figure 10 shows the PDFs and

**Table 3 The response errors of  $\delta L$  and the number of training samples by ASGC and SSGC. ASGC-1 ( $l_{max}=6, \epsilon_0=10^{-2}$ ), ASGC-2 ( $l_{max}=7, \epsilon_0=10^{-2}$ ), ASGC-3 ( $l_{max}=6, \epsilon_0=10^{-3}$ ), SSGC ( $l=6$ )**

	$\mathcal{E}_{ave}$	$\mathcal{E}_{rms}$	$N$
ASGC-1	$2.50 \times 10^{-3}$	$2.63 \times 10^{-2}$	23
ASGC-2	$2.63 \times 10^{-2}$	$2.13 \times 10^{-2}$	31
ASGC-3	$1.62 \times 10^{-3}$	$2.13 \times 10^{-2}$	57
SSGC	$1.62 \times 10^{-3}$	$2.12 \times 10^{-2}$	63
MCS	-	-	5000

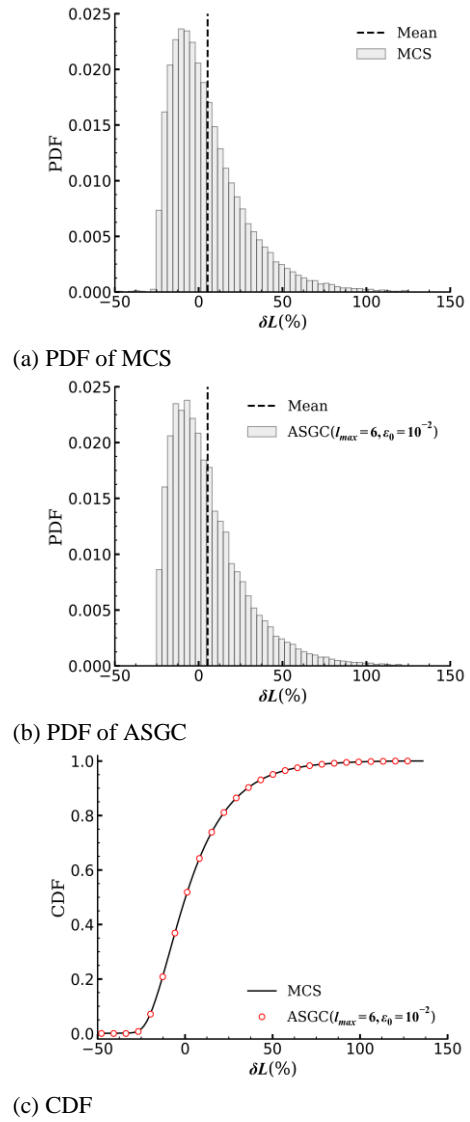


**Fig. 10. PDFs and CDFs for  $\delta L$ .**

CDFs of  $\delta L$  by direct MCS and ASGC. The PDF and CDF obtained by ASGC with  $l_{max}=6$  and  $\epsilon_0=10^{-2}$  are almost the same as those obtained by MCS, further illustrating the effectiveness of ASGC for the aerodynamic UQ study. Besides, the right-skewed PDFs demonstrate that the strong nonlinear dependence of performance changes on the incidence perturbations can be accurately evaluated by ASGC. In fact, the nonlinear dependence increases with  $\sigma_{\alpha}$ , which will be elaborated in the following study.

Through the above investigation on the response performance of ASGC, the aerodynamic UQ results can be derived from the ASGC model with  $l_{max}=6$  and  $\epsilon_0=10^{-2}$  efficiently and exactly. Subsequently, all aerodynamic UQ results were obtained using ASGC with  $l_{max}=6$  and  $\epsilon_0=10^{-2}$ . To analyze the effect of inlet incidences at different perturbation scales on the uncertainty of the changes for relative aerodynamic performance, five inlet incidence perturbation tolerances were set:  $\sigma_{\alpha} = 0.4, 0.6, 0.8, 1.0, 1.2$ . Meanwhile, four reference  $Ma_1=0.4, 0.5, 0.6, \text{ and } 0.7$

were assigned to investigate the effect of inlet incidence perturbations at different numbers of reference  $Ma_1$  on the uncertainty of the changes for relative aerodynamic performance.

Figure 11 shows the statistics of  $\delta L$  against the tolerance  $\sigma_\alpha$  at four reference Mach numbers. It can be observed that all the statistical mean values of  $\delta L$  are positive, i.e., the mean aerodynamic loss aggravates, which illustrates the importance of aerodynamic UQ in the inlet incidence perturbations at off-design incidences. Moreover, the overall variation trends of the statistics versus  $\sigma_\alpha$  at the four reference Mach numbers are similar. The mean values of  $\delta L$  exhibit evident quadratic increases with  $\sigma_\alpha$ , while the Stdvs exhibit nearly linear increases. Therefore,  $\delta L$  is the nonlinear dependence on the inlet incidence perturbation which gradually becomes greater with the increasing  $\sigma_\alpha$ . It implies that the PDFs of the aerodynamic performance changes will no longer meet the Gaussian distribution but deviate far away from it towards a large  $\sigma_\alpha$ . From Fig. 11, it can also be observed that as the reference  $Ma_1$  rises, the slopes  $d(\mu_{\delta L})/d(\sigma_\alpha)$  and

$d(\sigma_{\delta L})/d(\sigma_\alpha)$  increase, which shows stronger nonlinear dependence of  $\delta L$  on the inlet incidence perturbations. Therefore, the aerodynamic UQ concerning the inlet incidence perturbation at high reference  $Ma_1$  should be the top focus.

The variation law of PDF and CDF of  $\delta L$  versus the tolerance  $\sigma_\alpha$  at reference  $Ma_1 = 0.4, 0.5, \text{ and } 0.6$  is similar to that at reference  $Ma_1 = 0.7$ . Figure 12 presents the PDFs and CDFs of  $\delta L$  at reference  $Ma_1 = 0.7$ . It can be found that PDFs are more right-skewed with the increase of  $\sigma_\alpha$ . In the figure demonstrating CDFs, the arrows indicate the increasing directions of  $\sigma_\alpha$ . The high-end “tails” of  $\delta L$  become thicker as  $\sigma_\alpha$  increases, indicating that the maximum performance change increases with  $\sigma_\alpha$ . These results further confirm that the nonlinear dependence of performance changes on the inlet incidence perturbations becomes heavier with the increasing  $\sigma_\alpha$ .

Figure 13 compares the CDF of  $\delta L$  versus the tolerance  $\sigma_\alpha$  at four numbers of reference  $Ma_1$ . The CDF curves with the same  $\sigma_\alpha$  reveal that the

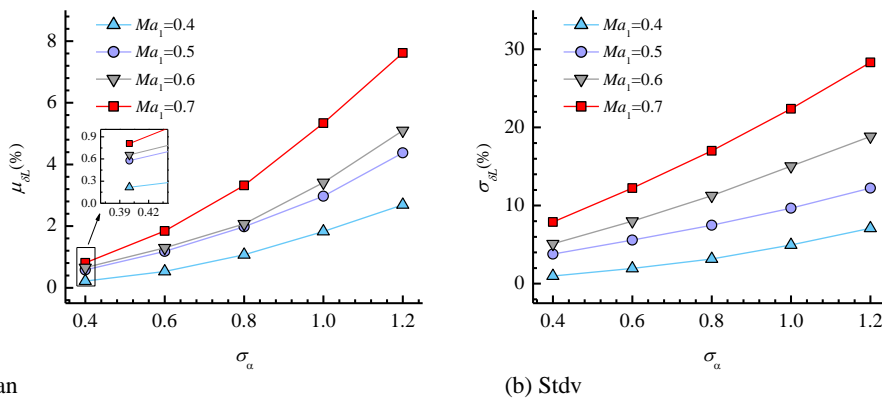


Fig. 11. Statistics of  $\delta L$  versus  $\sigma_\alpha$  at four numbers of reference  $Ma_1$ .

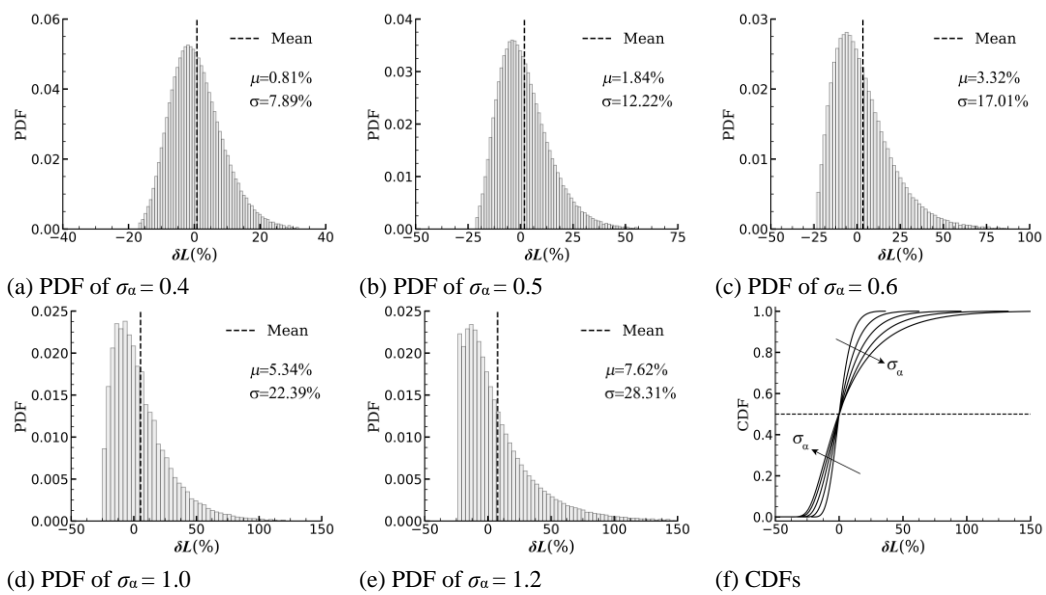
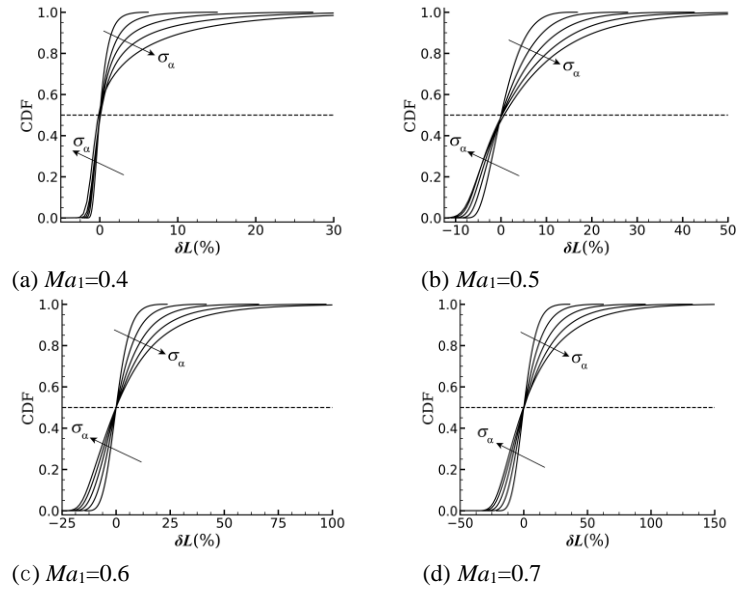


Fig. 12. PDFs and CDFs of  $\delta L$  versus  $\sigma_\alpha$  at reference  $Ma_1 = 0.7$ .



**Fig. 13.** CDF  $\delta L$  versus  $\sigma_\alpha$  at four numbers of reference  $Ma_1$ .

maximum performance change increases when the reference  $Ma_1$  rises, further confirming the strong nonlinear dependence of  $\delta L$  on the inlet incidence perturbations in the operating conditions of high reference performance.

### 3.3 Statistical Analysis of Flow Field

For the purpose of exploring the impact mechanisms of inlet incidence perturbations on the performance change of the cascade, the first two statistical moments of aerodynamic parameters of the flow field were calculated by  $N$  flow solutions. The calculation formulas for the statistical moments are similar to Eq. (12) and Eq. (13), and the  $N$  flow solutions are obtained by the ASGC ( $l_{max}=6$  and  $\omega=10^{-2}$ ) model. It should be noted that the deterministic impact of a variation of incidence on compressor performance had been studied (Goodhand 2010, Goodhand and Robert 2011) in-depth. Here, we intended to reveal the performance impact of incidence variations from the non-deterministic aspect.

Four typical cases were studied as shown in Table 4. Consistent with Section 3.2, this study involved the inlet incidence perturbations at  $\alpha=5$  deg. In Table 4, Cases 1 and 2 are used to explore the impact mechanisms of different perturbation scales on the performance uncertainty changes, while Cases 3 and 4 focused on the effect arising from different reference Mach numbers.

We first compared the statistical results of Cases 1 and 2. To reveal the influence law of incidence

**Table 4** Cases studied for statistical analysis of the flow field.

Case	1	2	3	4
$\sigma_\alpha$	0.4	1.0	1.2	1.2
$Ma_1$	0.7	0.7	0.4	0.6

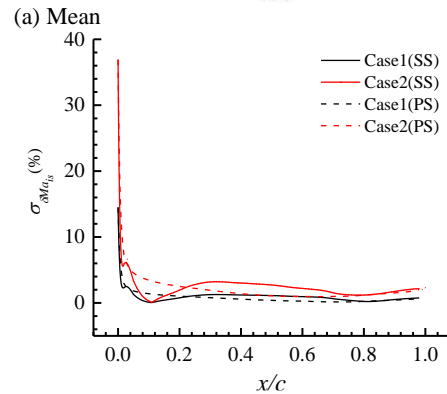
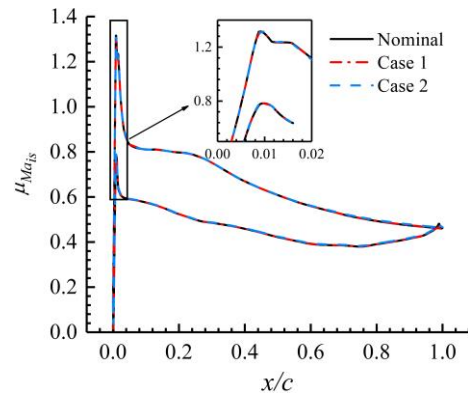


**Fig. 14.** Distributions of statistical results of  $Ma_{is}$  on blade surface for Cases 1 and 2.

perturbation scales on the blade surface flow, the distributions of the statistical results of  $Ma_{is}$  on the blade surface for Cases 1 and 2 were calculated as shown in Fig. 14. The nominal value indicates the results without concerning the inlet incidence perturbations. From Fig. 14(a), the  $\mu_{Ma_{is}}$  distributions of Cases 1 and 2 are almost duplicates of nominal ones, demonstrating that the influence of inlet incidence perturbations on the blade surface flow cannot be reflected by the statistical mean values of

aerodynamic parameters. Therefore, the influence should be evaluated by obtaining the variance. Figure 14(b) shows the Stdvs for the relative changes of isentropic Mach number  $\delta Ma_{is}$ . The definition of  $\delta Ma_{is}$  is:

$$\delta Ma_{is} = \frac{Ma_{is} - Ma_{is,0}}{Ma_{is,0}}, \quad (21)$$

where  $\delta Ma_{is,0}$  is the nominal isentropic Mach number. From the LE to about 0.1 chords, the inlet incidence perturbations lead to the sharp increment of  $\sigma_{\delta Ma_{is}}$  which is much higher than in other regions. It illustrates that the inlet incidence perturbations mainly affect the flow acceleration process near the LE. Most notably, the fluctuation of the flow acceleration significantly influences the aerodynamic load, due to the rapid diffusion process with strong reverse pressure gradients after the flow acceleration of the LE. Besides, the peak  $\sigma_{\delta Ma_{is}}$  near the LE of Case 2 increases dramatically compared with that of Case 1, illustrating that the flow acceleration near the LE is more significant with the increment of  $\sigma_{\alpha}$ .

To display the influence law of incidence perturbation scales on the passage flow, Fig. 15 presents statistical results of boundary layer shape factor  $H$  for Cases 1 and 2. The blue region represents the fluctuation range of  $H$ , the boundary of which is determined by the mean  $H$  minus one time's Stdv. The value of  $H$  represents the normalized boundary layer thickness and is useful to determine whether the boundary layer separation occurs. In the present study, the boundary layer separation occurs when  $H > 2.5$ . In Fig. 15, the fluctuation ranges of  $H$  in most regions on the PS are much smaller than those on the suction surface (SS), demonstrating that the incidence perturbations impose a weak effect on the boundary layer thickness on the pressure surface (PS).

However, the nominal  $H$  distributions on the SS in Figs. 15(a) and (b) illustrate that there are two local separations, i.e., LE and TE separations, in the region of the first 0.5 chords and 0.8 chords to 1.0 chords, respectively. It can be found that in the regions where the local separations occur, the mean  $H$  of Case 2 increases more with respect to the nominal than that of Case 1. The results show that due to the uncertainty perturbations of inlet incidences, the probability of the local separation scale relative to the nominal increases with  $\sigma_{\alpha}$ . Meanwhile, the fluctuation range of Case 2 is much larger than that of Case 1, demonstrating that the fluctuation of the local separation scales enhances when  $\sigma_{\alpha}$  increases. Figure 16 compares the Stdvs of entropy generation  $S_g$  between Case 1 and Case 2, which exactly illustrates that the uncertainty of the boundary layer separation and the wake mixing loss, resulting from the uncertainties of the local separations, increases with  $\sigma_{\alpha}$ .

Lastly, the statistical results of Cases 3 and 4 were compared. Figure 17 presents the statistical distributions of  $Ma_{is}$  on the blade surface for Cases 3 and 4. Similar to Figure 14, the statistical mean of  $Ma_{is}$  exhibits almost zero deviation from the nominal, and the increment of  $\sigma_{\delta Ma_{is}}$  is mainly centered in the first 0.1 chord region. These results further validate that the influence of inlet incidence perturbations on the cascade surface flow is majorly presented by the

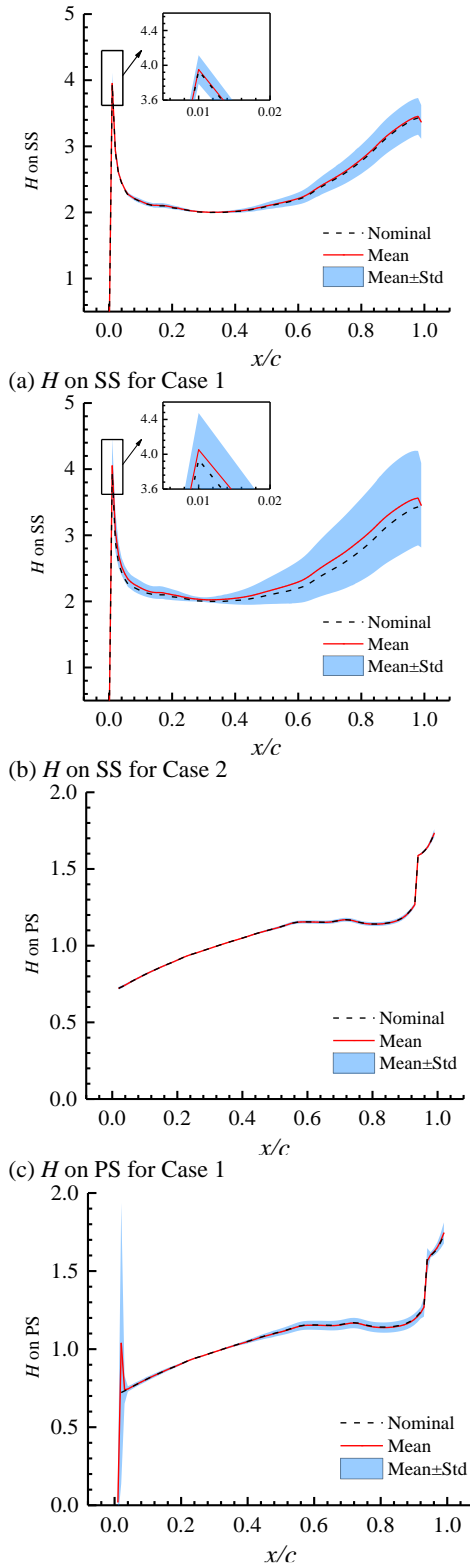
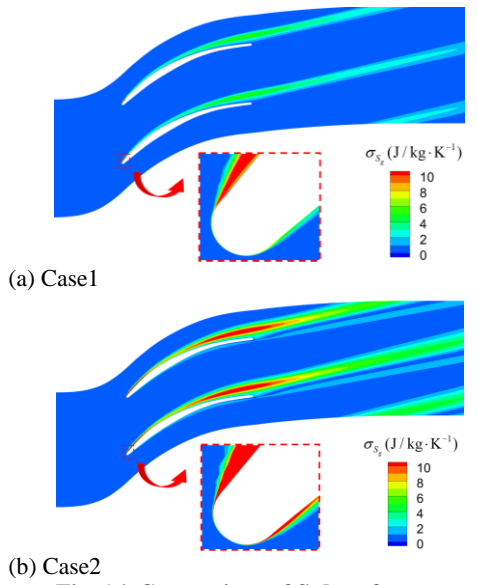
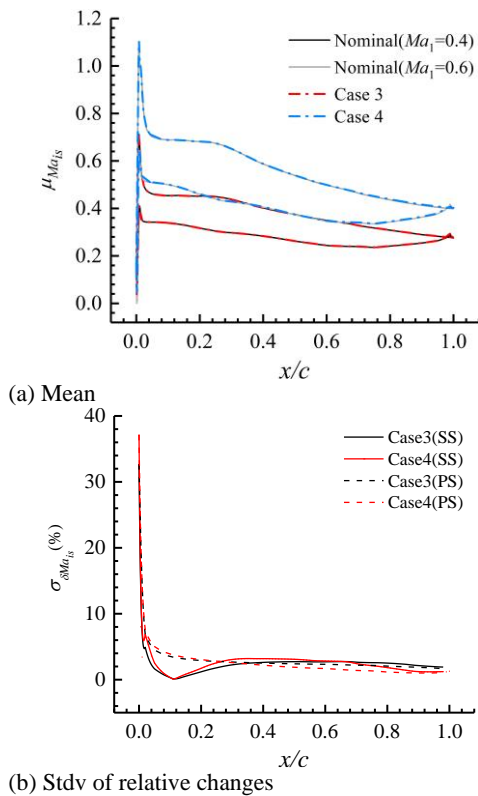


Fig. 15. Statistical results of the boundary layer shape factor for Cases 1 and 2.

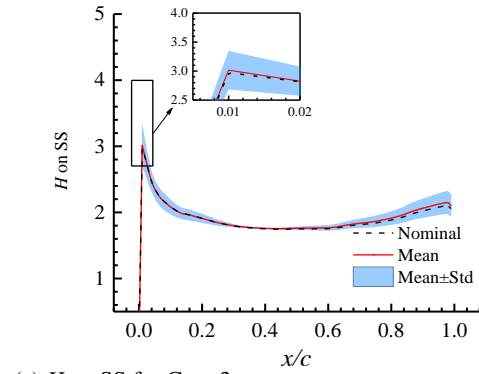
variance of the flow acceleration process near the LE. Moreover, the Stdvs of  $\delta Ma_{is}$  within the first 0.1 chords for Case 4 are larger than those for Case 3, manifesting that the flow acceleration process near the LE is more sensitive to the inlet incidence perturbations when the reference  $Ma_1$  is higher. Such variation law is not surprising because the results illustrated in Fig. 17(a) also show the nominal aerodynamic load near the LE advancing with the increment of the reference  $Ma_1$ , reflecting the increase of the sensitivity to the inlet incidence perturbations.



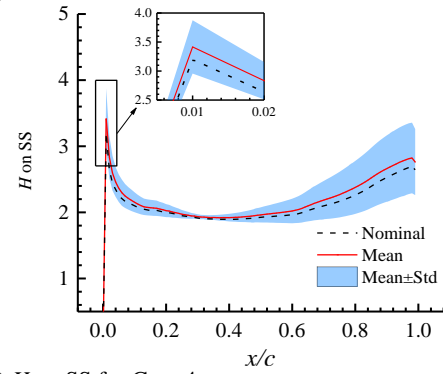
**Fig. 16. Comparison of Stdvs of entropy generation between Cases 1 and 2.**



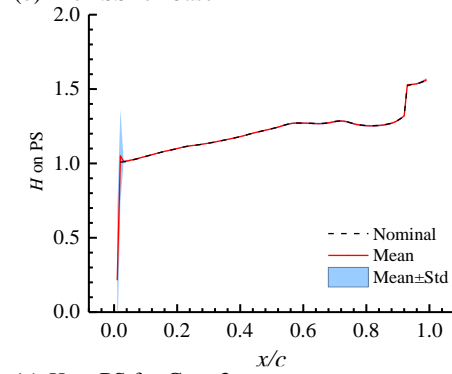
**Fig. 17. Distributions of statistical results of  $Ma_{is}$  on blade surface for Cases 3 and 4.**



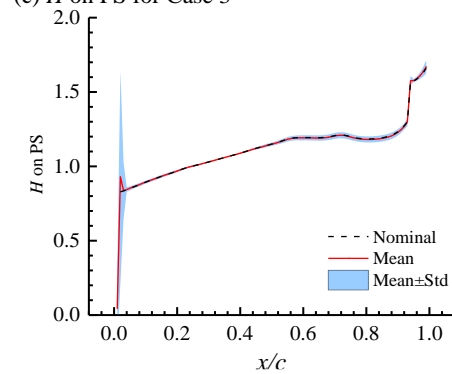
(a)  $H$  on SS for Case 3



(b)  $H$  on SS for Case 4



(c)  $H$  on PS for Case 3



(d)  $H$  on PS for Case 4

**Fig. 18. Statistical results of the boundary layer shape factor for Cases 3 and 4.**

Figure 18 gives the statistical results of  $H$  for Cases 3 and 4. The comparisons demonstrate that the boundary layer thickness on the SS is more sensitive to the perturbation of inlet incidences, since the fluctuation ranges of  $H$  in most regions on the PS are much smaller than those on the SS. As shown in Figures 18(a) and (b), the mean  $H$  distributions on

the SS indicate that there is a LE separation in Case 3, while there are LE and TE separations in Case 4. This is because the reference  $Ma_1$  in Case 4 is higher, the aerodynamic load near the LE is larger (See Figure 17(a)), and this situation is prone to induce the boundary layer separation on the SS. As such, it can be found that under the uncertainty perturbations of inlet incidences, the mean  $H$  on the SS for Case 4 increases compared to the nominal, while that for Case 3 is almost the same as the nominal. Meanwhile, the fluctuation range of Case 4 is much larger than that of Case 3, especially in the regions occurring the TE separation. Figure 19 presents the comparison of the Stdv of entropy generation between Cases 3 and 4. It shows that the uncertainty of the boundary layer separation and wake mixing losses increases with the increasing reference  $Ma_1$ .

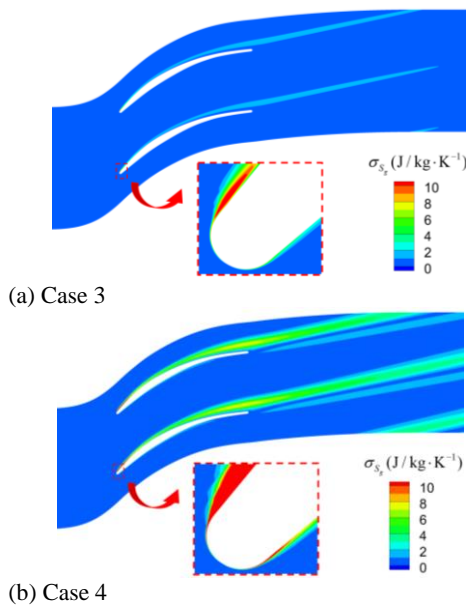


**Fig. 19. Comparison of Stdvs of entropy generation between Cases 3 and 4.**

According to the above analysis, the variation of the LE flow plays a leading role in the variation of aerodynamic performance when the inlet incidence is disturbed with uncertainties. The incidence perturbation will influence the Stdv of the flow acceleration near the LE of the SS, and subsequently cause dramatic fluctuations of the downstream boundary layer thicknesses, which will be more significant when there is a local separation. Under such circumstances, the Stdv of the separation and the wake mixing loss will inevitably be increased, and an uncertainty variation in aerodynamic performance appears. When the perturbation tolerance  $\sigma_a$  and the reference  $Ma_1$  rise, the Stdv of the flow acceleration near the LE increases, resulting in the increment of the mean and Stdv within the local separation scales. In summary, it is more significant to concern the shape optimization design near the LE for improving aerodynamic robustness concerning the random perturbations of the inlet incidence.

#### 4. CONCLUSION

To minimize the computational costs of highly accurate probabilistic surrogate modeling, the ASGC method was first introduced in the study, which can dynamically add nested collocation nodes with the increase of collocation levels. Compared with the direct MCS and the SSGC, the response performance for ASGC including the statistical accuracy and response accuracy is saved, while the model construction efficiency is significantly improved because of its nested adaptive sampling feature, which was validated and convinced by a highly nonlinear test function. Then for a controlled diffusion compressor cascade, the inlet incidence was assumed to be an uncertain parameter in truncated Gaussian distribution and, the uncertainty impact of the total pressure loss coefficient and flow field due to inlet incidence perturbations on the high reference incidence was quantified using the ASGC method.

The ASGC can effectively measure the effect of inlet incidence uncertainties on the controlled diffusion compressor cascade and the ASGC begins to be convergent to the result of the MCS method when  $l_{max}=6$  and  $\varepsilon_0=10^{-2}$ . The first two statistical moments of aerodynamic variables obtained by ASGC are in good agreement with those obtained by SSGC and MCS. The PDFs and CDFs of the response variable are easy to get from ASGC with accuracy, but a large number of samples are needed for MCS. Under the perturbations of inlet incidences, the mean aerodynamic loss always aggravates. It suggests that it is necessary to perform aerodynamic UQ concerning the inlet incidence perturbations at the off-design incidence. The mean values of  $\delta L$  exhibit evident quadratic enhancement with the increasing  $\sigma_a$ , while the Stdvs display nearly linear increases. Meanwhile, the PDF of  $\delta L$  deviates away from the Gaussian distribution and is more right-skewed with the increasing  $\sigma_a$ . It shows that the performance variations nonlinearly depend on the inlet incidence perturbations, and the nonlinear dependence becomes stronger when  $\sigma_a$  is growing. In addition, the slopes  $d(\mu_{\delta L})/d(\sigma_a)$  and  $d(\sigma_{\delta L})/d(\sigma_a)$  increase when the reference  $Ma_1$  climbs up, which reveals the greater nonlinear dependence of  $\delta L$  on the inlet incidence perturbations at high reference  $Ma_1$ .

The UQ of the flow field reveals that the variation of the LE flow takes the lead in the variation of aerodynamic performance when the inlet incidence is perturbed with uncertainty. The inlet incidence perturbation mainly influences the Stdv of the flow acceleration near the LE and subsequently causes dramatic fluctuations of the downstream boundary layer thicknesses, which will be more significant when there is a local separation. In addition, the Stdv of the flow acceleration near the LE increases with the perturbation tolerance  $\sigma_a$  and the reference  $Ma_1$ , resulting in the increment of the mean and Stdv of the local separation scales. Thus, the shape robustness optimization design near the LE should be deemed a priority for improving aerodynamic robustness concerning the inlet incidence perturbations.

## ACKNOWLEDGMENTS

The authors would like to acknowledge The National Major Science and Technology Project of China (Grant No. J2019-I-0011) and The Innovation Foundation for Doctor Dissertation of Northwestern Polytechnical University.

## REFERENCES

- Ahlfeld, R. and F. Montomoli, (2017). A single formulation for uncertainty propagation in turbomachinery: SAMBA PC. *Journal of Turbomachinery* 139(11), 111007.
- Bammert, K. and H. Sandstede (1976). Influence of manufacturing tolerances and surface roughness of blades on the performance of turbines. *Journal of Engineering for Gas Turbines and Power* 98(1), 29-36.
- Barthelmann, V., E. Novak and K. Ritter (2000). High dimensional polynomial interpolation on sparse grids. *Advances in Computational Mathematics* 12(4), 273-288.
- Bry, P., P. Laval and G. Billet (1985). Distorted flow field in compressor inlet channels. *Journal of Engineering for Gas Turbines and Power* 107(3), 782-791.
- Conrad, P. and Y. Marzouk (2013) Adaptive smolyak pseudospectral approximations. *SIAM Journal of Scientific Computing* 35(6), A2643-A2670.
- Garzon, V. E. and D. L. Darmofal (2003). Impact of geometric variability on axial compressor performance. *Journal of Turbomachinery* 125 (4), 692-703.
- Garzon, V. E. and D. L. Darmofal (2004). On the aerodynamic design of compressor airfoils for robustness under geometric uncertainty. In *Turbo Expo: Power for Land, Sea, and Air*, GT2004-53581.
- Genz, A. and B. D. Keister (1996). Fully symmetric interpolatory rules for multiple integrals over infinite regions with Gaussian weight. *Journal of Computational and Applied Mathematics* 71(2), 299-309.
- Gerstner, T. and M. Griebel (1998). Numerical integration using sparse grids. *Numerical Algorithms* 18, 209-232.
- Goodhand, M. N. (2010). *Compressor Leading Edges*. Ph. D. Thesis, University of Cambridge, England, Cambridge.
- Goodhand, M. N. and R. J. Robert (2011) Compressor leading edge spikes: a new performance criterion. *Journal of Turbomachinery* 133(2), 621-656.
- Gopinathrao, N. P., D. Bagshaw, C. Mabilat and S. Alizadeh (2009). Non-deterministic CFD simulation of a transonic compressor rotor. In *Turbo Expo: Power for Land, Sea, and Air*, GT2009-60122.
- Griebel, M. (1998). Adaptive sparse grid multilevel methods for elliptic PDEs based on finite differences. *Computing* 61, 151-179.
- Guo, Z. and W. Chu (2022). Stochastic aerodynamic analysis for compressor blades with manufacturing variability based on a mathematical dimensionality reduction method. *Proceeding of the Institution of Mechanical Engineers Part C: Journal of Mechanical Engineering Science* 236(10), 5719-5735.
- Guo, Z., W. Chu and H. Zhang (2022a). A data-driven non-intrusive polynomial chaos for performance impact of high subsonic compressor cascades with stagger angle and profile errors. *Aerospace Science and Technology* 129, 107802.
- Guo, Z., W. Chu and H. Zhang (2022b). Uncertainty analysis of global and local performance impact of inflow and geometric uncertainties using sparse grid-based non-intrusive polynomial chaos. *Proceeding of the Institution of Mechanical Engineers Part A: Journal of Power and Energy* 236(7), 1239 -1256.
- Heiss, F. and V. Winschel (2008). Likelihood approximation by numerical integration on sparse grids. *Journal of Econometrics* 144(1), 62-80.
- Hosder, S., R., Walters and M. Balch (2007). Sampling for non-intrusive polynomial chaos applications with multiple uncertain input variables. In: *48th AIAA/ASME/ASCE/AHS/ASC Structures, Structural Dynamics, and Materials Conference*, Conference Paper AIAA.
- Hosder, S., R. W. Walters and M. Balch (2010). Point-collocation nonintrusive PC method for stochastic computational fluid dynamics. *AIAA Journal* 48(12), 2721-2730.
- Lange, A., M. Voigt, K. Vogeler, H. Schrapp, E. Johann and V. Gümmer (2010). Probabilistic CFD simulation of a high-pressure compressor stage taking manufacturing variability into account. In *Turbo Expo: Power for Land, Sea, and Air*, GT2010-22484.
- Lange, A., M. Voigt, K. Vogeler, H. Schrapp, E. Johann and V. Gümmer (2012) Impact of manufacturing variability and nonaxisymmetry on high-pressure compressor stage performance. *Journal of Engineering for Gas Turbines and Power* 134(3), 032504.
- Liao, Q., D. Zhang and H. Tchelepi (2017). Nested sparse grid collocation method with delay and transformation for subsurface flow and transport problems. *Advances in Water Resources* 10, 158-173.
- Liu, Z., X. Wang and S. Kang (2014). Stochastic performance evaluation of horizontal axis wind

- turbine blades using non-deterministic CFD simulations. *Energy* 73, 126-136.
- Loeven, G. J. A. and H. Bijl (2010). The application of the probabilistic collocation method to a transonic axial flow compressor. In *51st AIAA/ASME/ASCE/AHS/ASC Structures, Structural Dynamics, and Materials Conference*, Conference Paper AIAA.
- Loeven, G. J. A., J. Witteveen and H. Bijl (2007). Probabilistic collocation: an efficient nonintrusive approach for arbitrarily distributed parametric uncertainties. In *45th AIAA Aerospace Sciences Meeting Exhibit*, pp. 8-11.
- Luo, J. and F. Liu (2018). Statistical evaluation of performance impact of manufacturing variability by an adjoint method. *Aerospace Science and Technology* 77, 471-484.
- Ma, C., L. Gao, Y. Cai and R. Li (2017). Robust optimization design of compressor blade considering machining error. In *Turbo Expo: Power for Land, Sea, and Air*, GT2017-63157.
- Ma, X. and N. Zabarvas (2009). An adaptive hierarchical sparse grid collocation algorithm for the solution of stochastic differential equations. *Journal of Computational Physics* 228(8), 3084-3113.
- Panizza, A., D. T. Rubino and L. Tapinassi (2014). Efficient uncertainty quantification of centrifugal compressor performance using polynomial chaos. In *Turbo Expo: Power for Land, Sea, and Air*, GT2014-25081.
- Putko, M. M., P. A. Newman, A. A. Taylor III and L. L. Green (2002). Uncertainty propagation and robust design in CFD using sensitivity derivatives. *Journal of Fluids Engineering* 124(1), 60-69.
- Roelke, R. J. and J. E. Haas (1983). The effects of rotor blade thickness and surface finish on the performance of a small axial flow turbine. *Journal of Engineering for Gas Turbines and Power* 105(2), 377-382.
- Seshadri, P., G. T. Parks and S. Shahpar (2015). Leakage uncertainties in compressors: the case of Rotor 37. *Journal of Propulsion and Power* 31(1), 456-466.
- Smoljak, S. A. (1963). Quadrature and interpolation formulae on tensor products of certain function classes. *Doklady Akademii Nauk SSSR* 4(5), 1042-1045.
- Stenning, A. (1980). Inlet distortion effects in axial compressors. *Journal of Fluids Engineering* 102 (1), 7-13.
- Wang, K., F. Chen, J. Yu and Y. Song (2020). Nested sparse-grid stochastic collocation method for uncertainty quantification of blade stagger angle. *Energy* 201, 117583.
- Wang, X. and Z. Zou (2019). Uncertainty analysis of impact of geometric variations on turbine blade performance. *Energy* 176, 67-80.
- Wu, X., W. Zhang, S. Song and Z. Ye (2017). Sparse grid-based polynomial chaos expansion for aerodynamics of an airfoil with uncertainties. *Chinese of Aeronautics* 31(5), 997-1011.
- Wunsch, D., C. Hirsch, R. Nigro and G. Coussement (2015). Quantification of combined operational and geometrical uncertainties in turbomachinery design. In *Turbo Expo: Power for Land, Sea, and Air*, GT2015-43399.
- Xia, Z., J. Luo and F. Liu (2019a). Performance impact of flow and geometric variations for a turbine blade using an adaptive NIPC method. *Aerospace Science and Technology* 90, 127-139.
- Xia, Z., J. Luo and F. Liu (2019b). Statistical evaluation of performance impact of flow variations for a transonic compressor rotor blade, *Energy* 189(15), 116285.
- Xiu, D. and G. Karniadakis (2003). Modelling uncertainty in flow simulations via generalized polynomial chaos. *Journal of Computational Physics* 187(1), 137-167.